




Twitching the inherent properties: the impact of transition metal Mn-doped on LaFeO₃-based perovskite materials

Ramesh Kumar Raji^{1,4,*} , Tholkappiyan Ramachandran², M. Muralidharan³, R. Suriakarthick⁴, M. Dhilip⁴, A. Raja⁴, Vishista Kurapati¹, Fathalla Hamed², P. Ramasamy⁴, and Abdel-Hamid I. Mourad^{5,6}

¹Department of Physics, College of Engineering, Guindy, Anna University, Chennai, Tamil Nadu 600025, India

²Department of Physics, College of Science, United Arab Emirates University, P.O. Box 15551, Al Ain, United Arab Emirates

³Department of Materials Science, University of Madras, Chennai, Tamil Nadu 600025, India

⁴SSN Research Centre, Sri Sivasubramaniya Nadar College of Engineering, Kalavakkam, Chennai, Tamil Nadu 603110, India

⁵Department of Mechanical Engineering, College of Engineering and National Water and Energy Center, United Arab Emirates University, P.O. Box. 15551, Al Ain, United Arab Emirates

⁶Mechanical Design Department, Faculty of Engineering, Helwan University, Cairo, Egypt

Received: 14 July 2021

Accepted: 12 September 2021

Published online:

24 September 2021

© The Author(s), under exclusive licence to Springer Science+Business Media, LLC, part of Springer Nature 2021

ABSTRACT

Perovskite structured materials have received a lot of attention recently due to their extraordinary characteristics. In this work, conventional solid-state reaction was adopted to synthesize perovskite-based lanthanum ferrite materials and studied their inherent properties with the influence of Mn concentrations. The materials were characterized by XRD, FTIR, Raman, SEM, EDS and mapping, UV-Vis, photoluminescence, dielectric, magnetic properties and the Mn ions were found to be incorporated into the lanthanum ferrite. Rietveld refinement results confirm that synthesized materials are single-phase orthorhombic structures with an average crystallite size of 80–67 nm. A broad excitation band around 360 to 450 nm with a maximum at 409 nm is attributed to the intra configurational f–f electronic transition of La³⁺. Mn-doping-induced great enhancement in the visible range of LaFeO₃ red luminescence. Mn-dopant has a significant influence on dielectric characteristics in the frequency ranges of 1 kHz and 1 MHz from 50 to 110 °C, which obey the Maxwell–Wagner polarization model and Koop’s phenomenological theory. The observation of weak ferromagnetism at 305 K in the *M–H* loop is considered to be the result of the intriguing exchange interaction between Fe/Mn and oxidation states. It is proposed that LaMn_{*x*}Fe_{1–*x*}O₃ (*x* = 0.05–0.25) materials with varying characteristics could be developed to satisfy a diversity of requirements.

Address correspondence to E-mail: rameshkumarphy93@gmail.com

1 Introduction

Technological evolution and concurrent demand for reducing the sizes of various crucial electronic equipment including transistors have made stronger the research towards multifunctional materials [1]. Among these, perovskite structured materials are an important class of functional materials that has stimulating structural, electrical, and magnetic properties. It has the chemical formula ABO_3 (where A is a rare-earth element and B is a 3d transition metal) and is fortunate for its cutting-edge use in advanced technologies such as sensors, solid oxide fuel cells, information storage devices, spintronics, microelectronics, magnetic applications, catalysts, and so on [2–8]. The physical properties of these perovskites are dependent on numerous factors such as synthesis technique, chemical composition, sintering temperature with time, and substitution of different cations. The rare-earth *orthoferrites* ($RFeO_3$) are the class of material that has a wide variety of applications in memory-based devices. Some $RFeO_3$ materials having excellent magneto-optical properties can be applied to make magneto-optical sensors, magneto-optical switches, and other devices [9, 10].

Lanthanum ferrite ($LaFeO_3$) is a notable perovskite material with an orthorhombic structure and canted antiferromagnetic nature at a high Neel temperature of 740 K [11]. It has established much attention due to its electrical and multifaceted magnetic properties with the connection between spin, charge, and orbital degrees of freedom. Fascinatingly, multiferroic properties in the $LaFeO_3$ system have been reported by Acharya et al. [11]. Several alterations in $LaFeO_3$ have recently been developed to improve its multifunctional characteristics. Artificial superlattices of $LaMnO_3$ – $LaFeO_3$ perceived that the magnetic response could be controlled by changing the order of Mn and Fe ions in the host lattice were reported by Ueda and Tabata Hand Kawai [12]. On the other hand, Zhi-Xian Wei et al. were synthesized $LaFeO_3$ and $LaFe_{0.5}Mn_{0.5}O_{3-\delta}$ by solution combustion method using stearic acid and studied their magnetization and photocatalytic activity [13]. R. Dhahri et al. studied the structural and electrical properties of $La_{1-x}A_xMnO_3$ compounds ($x = 0.05$ – 0.20) by the sol–gel technique and reveals that the existence of mixed valences Mn^{3+} – Mn^{4+} encourages both ferromagnetic state and metallic conductivity [14]. P.P. Hankare et al. were prepared a $LaMn_xFe_{1-x}O_3$

($1.0 \geq x \geq 0$) compound using a sol–gel auto combustion method that demonstrated the semiconducting nature [15]. $LaMn_{0.5}Fe_{0.5}O_3$ nanocrystalline powders exhibited considerable dielectric properties prepared via a polyvinyl alcohol sol–gel method [16] by Chunlian Zenga et al. using an auto combustion route Shovan Kumar Kundu et al. were synthesized Mn-doped $LaFeO_3$ revealed an improvement in multiferroic and dielectric properties owing to Mn-doping in Fe site [1]. Jung-Hoon Jeong et al. have been reported on Mn-doping in $LaFeO_3$ exhibit improvement in the magnetic moment and the control of the coercive field from the antiferromagnetic $LaFeO_3$ [17]. Tong et al. described $LaMn_{1-x}Fe_xO_3$ ($x = 0$ to 0.4) system exhibited that there is a certain prospect of the double exchange interaction between Fe^{3+} and Mn^{3+} ions [18].

Based on these findings, it is clear that the influence of synthesis processes and doping conditions can change the crystalline phase and surface morphology of this system, hence controlling the intrinsic properties of $LaFeO_3$ materials. The conventional solid-state reaction (SSR) or high-temperature synthesis approach has unique advantages. Hence, we address such approaches to synthesize $LaFe_{1-x}Mn_xO_3$ ferrite materials and studied their inherent properties like structural, electrical, optical, and magnetic by the influence of Mn-doping conditions. The properties of $LaMn_xFe_{1-x}O_3$ ferrite materials were characterized using powder X-ray diffraction (XRD)–Rietveld refinements, Raman spectroscopy, Fourier transform infrared (FT-IR) analysis, scanning electron microscopy with energy dispersive X-ray analysis, UV–Vis spectroscopy, photoluminescence, dielectric and magnetization technique, and the results are analyzed and reported.

2 Experimental section

2.1 Materials and methods

The polycrystalline bulk materials of $LaMn_xFe_{1-x}O_3$ ($x = 0.05$ – 0.25) were synthesized using the conventional solid-state reaction technique (SSR). As starting materials, stoichiometric amounts of high purity ($> 99.9\%$) lanthanum oxide (La_2O_3), iron oxide (Fe_2O_3), and manganese oxide (MnO_2) powders were utilized.

The stoichiometric amount of selected precursors were batch weighed with their proportion. The weighed precursors were subsequently transferred to an agate mortar and well-grounded using pestle for 30 min. The grounded samples were again stirred using acetone as a grinding medium for 45 min until to produce uniform fine powders. To achieve a better homogeneity powder, the fine powders were moved to a box furnace operating at 900 °C for 12 h, 1000 °C for 6 h, and 1200 °C for 6 h before being allowed to cool to ambient temperature at a rate of 5 °C/min. The final fine powders were removed from the box furnace and ground well for 15 min and hence stored for further characterization.

2.2 Characterization techniques

All the synthesized perovskite-type-LaMn_xFe_{1-x}O₃ ($x = 0.05$ to 0.25) ferrite materials are characterized with room temperature. Powder X-ray diffraction (XRD) profiles were examined using Bruker D2 PHASER set to 40 kV and a current of 30 mA. The profiles were taken using the Cu K α X-ray line of 1.5418 Å over a 20° to 60° range with a step size of 0.02°/min. The XRD profiles were checked for phase identification against the International Center for Diffraction Data (ICDD) PDF-2 database. The analysis of Rietveld refinements was carried out using FULL PROF software of the recorded XRD profiles. A pseudo-Voigt profile function was used to describe the diffraction peaks, with a Lorentzian contribution to the Gaussian peak shape. FT-IR spectra were collected in the 500–4000 cm⁻¹ range using a BRUKER ALPHA FT-IR Spectrophotometer using opus 7.2 software. Raman spectra were obtained over the range of 100–1000 cm⁻¹ with an HR 800 UV spectrophotometer equipped with a Horiba Jobin-Yvon, excitation He-Ne laser source at $\lambda = 488$ nm. The microstructure of the produced ferrite materials was investigated using a JEOL JSM-6010LA scanning electron microscopy (SEM) apparatus set to 20 keV accelerating voltage. Secondary electron imaging (SEI) was used to collect SEM images. An energy dispersive X-ray spectrometer was used to perform element mapping and quantitative analysis (EDS). The UV-Vis absorption spectra were studied using a Perkin-Elmer spectrometer with a wavelength source of 200–800 nm. The photoluminescence spectra were analyzed using Horiba Jobin-Yvon-Fluoromax 4 spectrofluorometer. The temperature, as well as the

frequency dependence dielectric studies, were studied by Wayne Kerr-LCR 4275 instrument having a frequency range of 10 Hz to 1 MHz and a temperature range of 50 to 110 °C. The prepared pellet materials were prudently polished and silver-coated on both faces which act as electrodes for the dielectric spectroscopy measurements. The magnetic properties of the produced ferrite materials were investigated using a Lakeshore (Model-7404) vibrating sample magnetometer with a maximum magnetic field of 15 kOe.

3 Results and discussion

3.1 Structural phase analysis

Powder X-ray diffraction examinations at ambient temperature were used to determine the phase identification of the produced perovskite-type-LaMn_xFe_{1-x}O₃ ($x = 0.05$ to 0.25) ferrite materials. Figure 1 shows powder XRD profiles of the LaMn_xFe_{1-x}O₃ ($x = 0.05$ to 0.25) ferrite samples. All the diffraction planes are indexed and identified with an orthorhombic phase of standard data (JCPDS card No. 37-1493) with a space group of *Pbnm*. The broadening of diffraction peaks suggests that the ferrite materials generated are made up of fine crystallites. Notably, as seen in Fig. 1f, the (121) plane migrated toward the right angle when Mn concentration increased in LaFeO₃, indicating the presence of lattice distortions in the composition. As a result, Rietveld refinement analysis was performed on all of the ferrite materials to confirm the distortion. The Rietveld refined profiles of perovskite-type-LaMn_xFe_{1-x}O₃ ($x = 0.05$ to 0.25) ferrite materials are shown in Fig. 1a–e). Table 1 shows the improved values of lattice parameters, bond distance, reliability factors (W_p and W_{Rp}), bond angle, and χ^2 for synthesized ferrite materials. Table 1 shows the decreased tendencies toward lattice parameters acquired from Rietveld refinements. This could be due to the ionic radius of Mn³⁺/Mn⁴⁺ (0.58/0.53 Å) is substantially less than that of Fe³⁺ (0.645 Å) [20]. The obtained lattice constants correlate well with those published in the literature [19]. Furthermore, the typical crystallite sizes were determined using the Scherrer equation [21].

$$D = 0.9\lambda/\beta \cos \theta \quad (1)$$

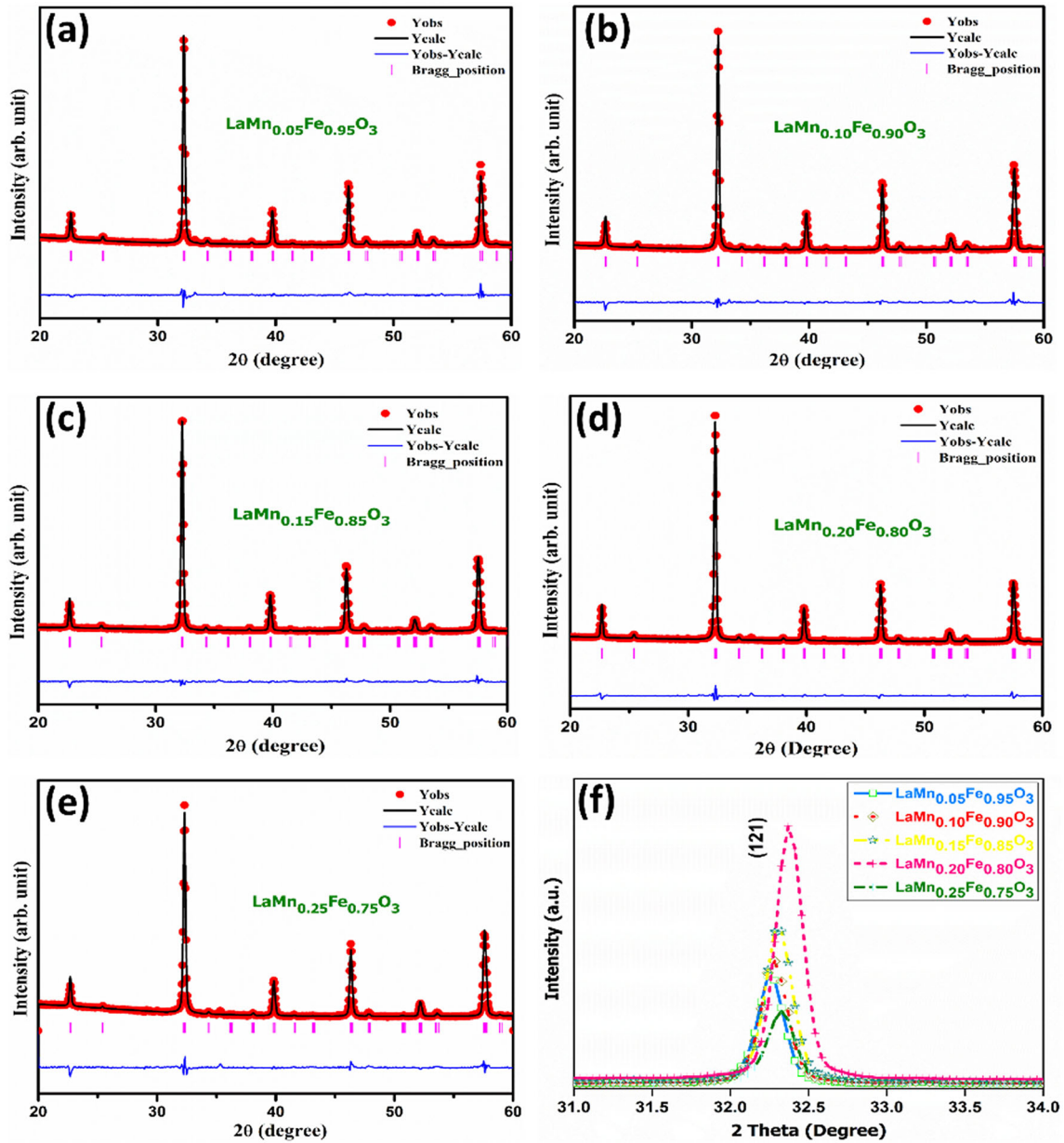


Fig. 1 Rietveld refinement XRD profiles (a–e) and enlarged view of (121) high intensity peak (f) of the synthesized LaMn_xFe_{1-x}O₃ ($x = 0.05–0.25$) ferrite materials via conventional solid-state

reaction. Blank curve: observed pattern, red curve: calculated pattern, blue curve: difference pattern

where D denotes the average crystallite size, λ is the X-ray wavelength (1.5405×10^{-10} m), β is the full width at half maximum intensity, and θ is the Bragg’s diffraction angle. Table 1 summarizes the determined average crystallite size, D . The values are comparable to those reported for LaFeO₃ [1]. The average crystallite size was found to be smaller in the table, which is attributable to the substitution of Fe cation by Mn ions. The crystallite size of ferrite material is usually

determined by the porosity, sintering temperature, and diffusivity of the individual grains. It is possible that the doping of Mn ions into the Fe³⁺ (B-site) of the LaFeO₃ lattice hinders grain development during the SSR process in this scenario.

3.2 FT-IR studies

Figure 2 depicts the recorded FTIR spectra of the perovskite-type-LaMn_xFe_{1-x}O₃ ($x = 0.05–0.25$) ferrite

Table 1 Structural constraints, bond angle and bond length of the synthesized $\text{LaMn}_x\text{Fe}_{1-x}\text{O}_3$ ($x = 0.05\text{--}0.25$) ferrite materials as tabulated from the Rietveld analysis

Structural parameters	$x = 0.05$	$x = 0.10$	$x = 0.15$	$x = 0.20$	$x = 0.25$
a (Å)	5.5570	5.5541	5.5559	5.5376	5.5520
b (Å)	5.5598	5.5524	5.5457	5.5493	5.5452
c (Å)	7.8558	7.8472	7.8377	7.8511	7.8303
Volume	242.70	242.00	241.48	241.26	240.63
W_{Rp} (%)	14.0	13.7	10.0	8.77	14.7
W_{p} (%)	10.4	10.3	8.16	7.56	10.9
χ^2	4.71	5.59	5.62	7.60	5.01
α	90	90	90	90	90
β	90	90	90	90	90
γ	90	90	90	90	90
Crystallite size (nm)	80	79	76	75	67
Bond distance (Å)					
Fe–O(1)	2.039 (23)	1.98 (4)	1.90 (5)	1.96 (7)	1.96 (6)
Fe–O(2)	2.000 (15)	2.034 (16)	2.002 (19)	2.17 (5)	2.020 (16)
Bond angle (°)					
Fe–O ₁ –Fe	156.6 (7)	159.9 (12)	156.8 (17)	164.0 (24)	157.6 (17)
Fe–O ₂ –Fe	153 (4)	149.0 (33)	156 (5)	158 (4)	158 (4)

materials over the wavelength range $500\text{--}4000\text{ cm}^{-1}$ at ambient temperature. The asymmetric C–H stretching vibrational mode is responsible for the observed adsorption band around 2900 cm^{-1} . The asymmetric bending vibration of the atmospheric CO_2 group is represented by the band near 2350 cm^{-1} . The most powerful bands, which emerge in the $500\text{--}650\text{ cm}^{-1}$ range, were attributed to stretching vibrations at the Fe–O bond in the octahedral MO_6 structure, where the wavenumber and intensity depend on the nature of the cations distribution and their occupancy in the perovskite-type sublattices [22]. In this scenario, the increase in Mn concentration causes a minor shift in vibrational

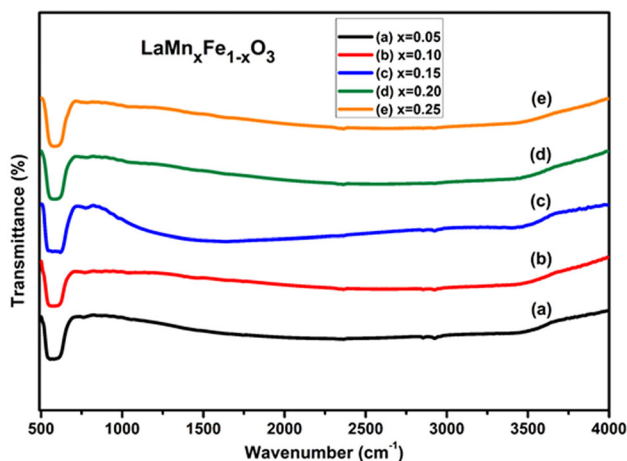


Fig. 2 FTIR spectrum of the synthesized $\text{LaMn}_x\text{Fe}_{1-x}\text{O}_3$ ($x = 0.05\text{--}0.25$) ferrite materials

bands toward lower wavenumbers. This could be attributable to flaws in the perovskite structures, which cause a drop in the lattice constant, as proven by the XRD investigation. Nonetheless, the slight variations in band locations indicate that the bond angle and bond length have changed (Table 1).

3.3 Raman studies

Figure 3 depicts a series of typical Raman spectra in the $100\text{--}1000\text{ cm}^{-1}$ range for $\text{LaMn}_x\text{Fe}_{1-x}\text{O}_3$ ($x = 0.05\text{--}0.25$) ferrite materials with varying Mn-doping levels. The consistent change in vibrational spectra can be attributed to a change in the local atomic structure caused by the presence of Mn ions in the LaFeO_3 material. The observed $\text{LaMn}_x\text{Fe}_{1-x}\text{O}_3$ ($x = 0.05\text{--}0.25$) ferrite materials have an orthorhombic structure ($Pb\text{-}nm$ space group). The group theory investigation for the following modes is represented as [23],

$$\begin{aligned} \Gamma_{\text{opt}(Pbnm)} = & (\text{R})7A_g + (\text{R})7B_{1g} + (\text{R})5B_{2g} + (\text{R})5B_{3g} \\ & + (\text{S})8A_u + (\text{IR})7B_{1u} + (\text{IR})9B_{2u} + (\text{IR})9B_{3u} \\ & + (\text{ac})B_{1u} + (\text{ac})B_{2u} + (\text{ac})B_{3u} \end{aligned} \quad (2)$$

Only 24 of the 60 normal modes predicted by group theory are Raman active (A_g , B_{1g} , B_{2g} , and B_{3g} symmetry).

$$\Gamma_{\text{Raman}(Pbnm)} = 7A_g + 7B_{1g} + 5B_{2g} + 5B_{3g} \quad (3)$$

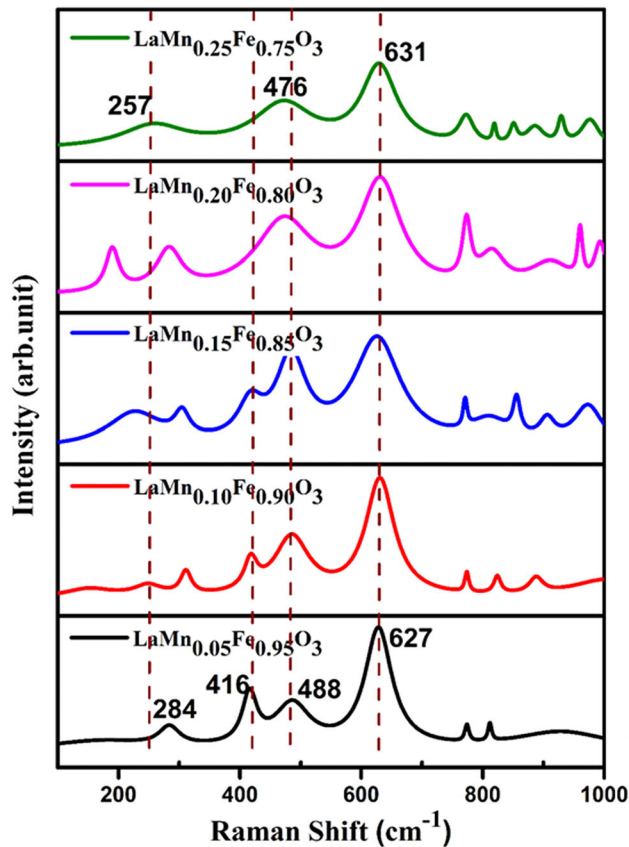


Fig. 3 Raman spectra of the synthesized $\text{LaMn}_x\text{Fe}_{1-x}\text{O}_3$ ($x = 0.05\text{--}0.25$) ferrite materials. The dotted lines represent the peaks that shifted/overlapped

There are only 24 Raman active modes and 25 IR modes in the orthorhombic structure ($Pbnm$ space group) (B_{1u} , B_{2u} , and B_{3u} symmetry). Where R, S, ac, and IR represent Raman, silent, acoustic modes, and infrared, respectively. Table 2 lists the Lorentzian individual components, the peak location of each component, i.e., the natural frequency (cm^{-1}) of each Raman active mode seen in Fig. 4, as well as the respective Raman active modes.

Figure 4 shows the Raman active modes at 158, 284, 416, 488, 627, 774, 813 and 926 cm^{-1} . The four-strong modes found at 284, 416, 488, and 627 cm^{-1} , 488, and 627 cm^{-1} strong modes are assigned to A_g symmetry. The B_{1g} symmetry is attributed to the remaining modes at 284, 416 cm^{-1} . The A–O bonds are related to lower-order frequency Raman modes, whereas the B–O bonds are associated with higher-order frequency modes [24]. The measured Raman active modes accord well with previous publications [25–27] on the perovskite structure compound. The strong absorption modes of Mn (0.05) ion at 158 cm^{-1}

were systematically shifted to 224 cm^{-1} , confirming the substantial impact of Mn (0.15) ion in the Le–O lattice. In addition, a shift in the position of intense Raman signals as depicted in Fig. 3 with dotted lines. This might be due to an increase in the Mn concentration range ($x = 0.05\text{--}0.25$); the modes do not present in the same way for frequencies, intensities, and widths; and there is no structural phase transition, as determined by XRD. This happens due to some modes are more sensitive to tolerance factors, while others are more sensitive to B-site ordering, which has differing consequences on the modes. In contrast, the B_{1g} -like modes in the neighborhood of 416 cm^{-1} (associated with B/O site ion motions) tend to merge with increasing Mn substitution (x). In this situation, the broad higher frequency order two phonon vibration modes can be formed into five active modes peaking at 906, 926, 958, 971, and 991 cm^{-1} , i.e., observed in the double energy values of A_g and B_g normal modes present in Mn-doped LaFeO_3 compounds. Higher-order frequency (above 900 cm^{-1}) Raman active modes A_g and B_{2g} relate to the movement of oxygen atoms along the B–O axis, and their frequency is principally influenced by bonding forces and the B–O distance [28].

3.4 Surface morphology and compositional analysis

The surface morphologies of the synthesized $\text{LaMn}_x\text{Fe}_{1-x}\text{O}_3$ ($x = 0.05\text{--}0.25$) ferrite materials were characterized by a scanning electron microscope (SEM). The SEM micrographs of the synthesized $\text{LaMn}_x\text{Fe}_{1-x}\text{O}_3$ ($x = 0.05\text{--}0.25$) ferrite materials are shown in Fig. 5a–e. It is perceived that the nanosized particles have spherical shaped morphology and are slightly agglomerated. This could be explained by the magnetic interaction of the particles. The presence of La, Fe, Mn, and O elements is confirmed by EDS spectra analysis of the materials, as shown in Fig. 5. Other elements were not discovered within the detection range of our detector. Theoretically, the atomic percentages for La, Fe, and O should be 20%, 20%, and 60%, respectively. The atomic ratio of La/Fe increases in the current study, and it is 1.09, 1.13, 1.20, 1.26, and 1.29 when Mn-dopant concentrations increase. These are far from stoichiometric ratios. This suggests that ferrite materials appear to be richer in La and O deficient, which may result in some faults. $\text{La}_{1+x}\text{Fe}_{1-x}\text{Mn}_x\text{O}_{3-x}$ is the best way to express

Table 2 Symmetry assignments of the synthesized $\text{LaMn}_x\text{Fe}_{1-x}\text{O}_3$ ($x = 0.05\text{--}0.25$) ferrite materials

Details of the compounds and symmetry assignments				
$\text{LaMn}_{0.05}\text{Fe}_{0.95}\text{O}_3$	$\text{LaMn}_{0.10}\text{Fe}_{0.90}\text{O}_3$	$\text{LaMn}_{0.15}\text{Fe}_{0.85}\text{O}_3$	$\text{LaMn}_{0.20}\text{Fe}_{0.80}\text{O}_3$	$\text{LaMn}_{0.25}\text{Fe}_{0.75}\text{O}_3$
158: A_g	158: A_g	224: A_g	189: A_g	257: A_g
284: B_{1g}	247: A_g	303: A_g	286: B_{1g}	476: B_{3g}
416: B_{1g}	313: B_{3g}	416: B_{1g}	476: B_{3g}	631: B_{1g}
488: A_g	416: B_{1g}	488: A_g	627: A_g	774: A_g
627: A_g	488: B_{3g}	627: A_g	774: A_g	813: B_{1g}
774: A_g	627: A_g	770: B_{1g}	813: B_{1g}	856: A_g
813: B_{1g}	774: A_g	809: B_{1g}	906: $2B_{1g}$	885: B_{1g}
926: $2B_{2g}$	825: B_{1g}	856: A_g	958: $2A_g$	926: $2B_{2g}$
	885: B_{1g}	906: $2B_{1g}$	991: $2A_g$	971: $2A_g$
	991: $2A_g$	971: $2A_g$		

the molecular formula. The elemental makeup of the produced ferrite materials was influenced by the Mn-dopant. As indicated in the EDS mapping pictures in Fig. 6, a homogeneous distribution of comparable La, Fe, Mn, and O elements was detected in all of the manufactured materials. In the EDS mapping, each color corresponds to a single energy line emission for each element.

3.5 UV–Vis absorption spectroscopic analysis

The optical band gap energies of the synthesized $\text{LaMn}_x\text{Fe}_{1-x}\text{O}_3$ ($x = 0.05\text{--}0.25$) ferrite materials were investigated via UV–Vis spectroscopy. The UV–Vis absorption spectra of perovskite-based $\text{LaMn}_x\text{Fe}_{1-x}\text{O}_3$ ($x = 0.05\text{--}0.25$) are displayed in Fig. 7 (left side). For the synthesized materials, an excitonic absorption performance in the visible range of 200–500 nm is linked to the electronic transition from O-2p orbitals in the valence band to Fe-3d orbitals in the conduction band. The visible light region observed in the synthesized ferrite materials may make them useful for photocatalysts [29]. The optical band gap energy for the synthesized materials can be determined using the Tauc expression [30],

$$\alpha = A(h\nu - E_g)^n/h\nu \quad (4)$$

where α represents the absorption coefficient, ν denotes the frequency, h stays the Planck's constant, E_g represents the optical bandgap energy of the incident photon, A is a constant that is related to the transition probability, and n is related to the nature of the optical absorption transition. The value of n is 1/2 for direct permissible electronic transition (direct bandgap) and 2 for indirect allowable electronic

transition (indirect bandgap). The E_g values of the synthesized $\text{LaMn}_x\text{Fe}_{1-x}\text{O}_3$ ($x = 0.05\text{--}0.25$) ferrite materials were calculated by extrapolating the linear component of the plots of $(\alpha h\nu)^2$ against photon energy $h\nu$ (eV) for the direct as shown in Fig. 9 (right side). The E_g energy values found ranged from 2.86 to 3.40 eV. These values correspond well with Swatsitang et al. [31] reported value of 2.2 eV for lanthanum ferrite nanoparticles made through the sol–gel process. Generally, the E_g is affected by various factors such as strain, average crystallite size, morphology, lattice deformations, and the presence of impurities. In this study, the values of E_g are increased with Mn substitution in $\text{LaMn}_x\text{Fe}_{1-x}\text{O}_3$ ($x = 0.05\text{--}0.25$). This rise in the E_g of synthesized $\text{LaMn}_x\text{Fe}_{1-x}\text{O}_3$ ($x = 0.05\text{--}0.25$) ferrite compounds is consistent with the corresponding blue shifts in the absorption edges shown in Fig. 9 (right side). The increase in E_g values with corresponding drops in average crystallite size appears to be connected to some flaws within the perovskite structure, resulting in a decrease in the lattice, which is manifest from XRD results. As a result of the defects in the structures, some microstrain is produced, causing a difference in the ionic radii of Mn^{3+} and Fe^{3+} ions. In the current investigation, the ionic radius of Fe^{3+} ions (0.645 Å) is higher than that of Mn^{3+} ions (0.58 Å), hence E_g values rise [20]. This will allow the fabrication of $\text{LaMn}_x\text{Fe}_{1-x}\text{O}_3$ ($x = 0.05\text{--}0.25$) ferrite materials with varying optical band gaps. The ability to change the optical band gap by simply adjusting the concentration of Mn ($x = 0.05\text{--}0.25$) substitution may make these $\text{LaMn}_x\text{Fe}_{1-x}\text{O}_3$ ferrite materials appealing for photocatalytic and sensing applications.

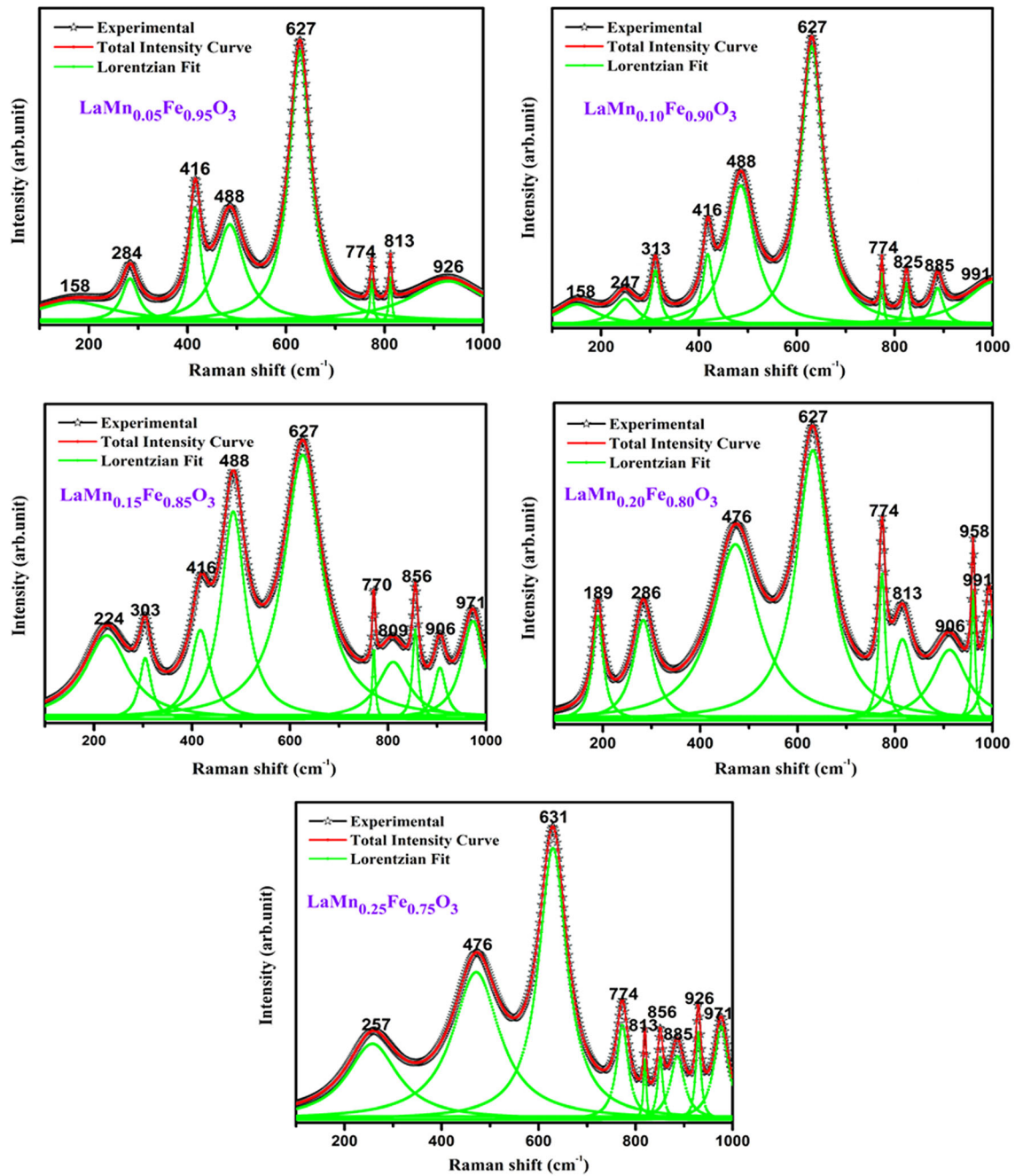


Fig. 4 Fitting curves of the Raman signal of the synthesized $\text{LaMn}_x\text{Fe}_{1-x}\text{O}_3$ ($x = 0.05\text{--}0.25$) ferrite materials with Lorentzian fitting curves. The black lines with shapes are experimental data, the solid curves with red shade with shapes are the total intensities of the Lorentzian lines and the green lines with shapes are the fitting of Lorentzian shapes

3.6 Photoluminescence property

Figure 8 depicts the excitation and emission spectra (inset) of the produced $\text{LaMn}_x\text{Fe}_{1-x}\text{O}_3$ ($x = 0.05\text{--}0.25$) ferrite materials. The spectra of photoluminescence excitation were obtained by monitoring the characteristic emission of La^{3+} ions at 409 nm (${}^3\text{P}_2 \rightarrow {}^1\text{S}_0$).

strong curves with green shade with shapes are the fitting of Lorentzian shapes and the solid curves with red shade with shapes are the total intensities of the Lorentzian lines

As shown in Fig. 8 (inset view), several excitation peaks appear across the broad range of excitation spectra from 370 to 450 nm, with a broad excitation peak from 397 to 450 nm centered at 397 nm that corresponds to the charge transfer transition (CTB), as well as the characteristic excitation peaks of La^{3+} ions at 370 nm, 397 nm, and 434 nm (${}^1\text{S}_0 \rightarrow {}^3\text{P}_2$);

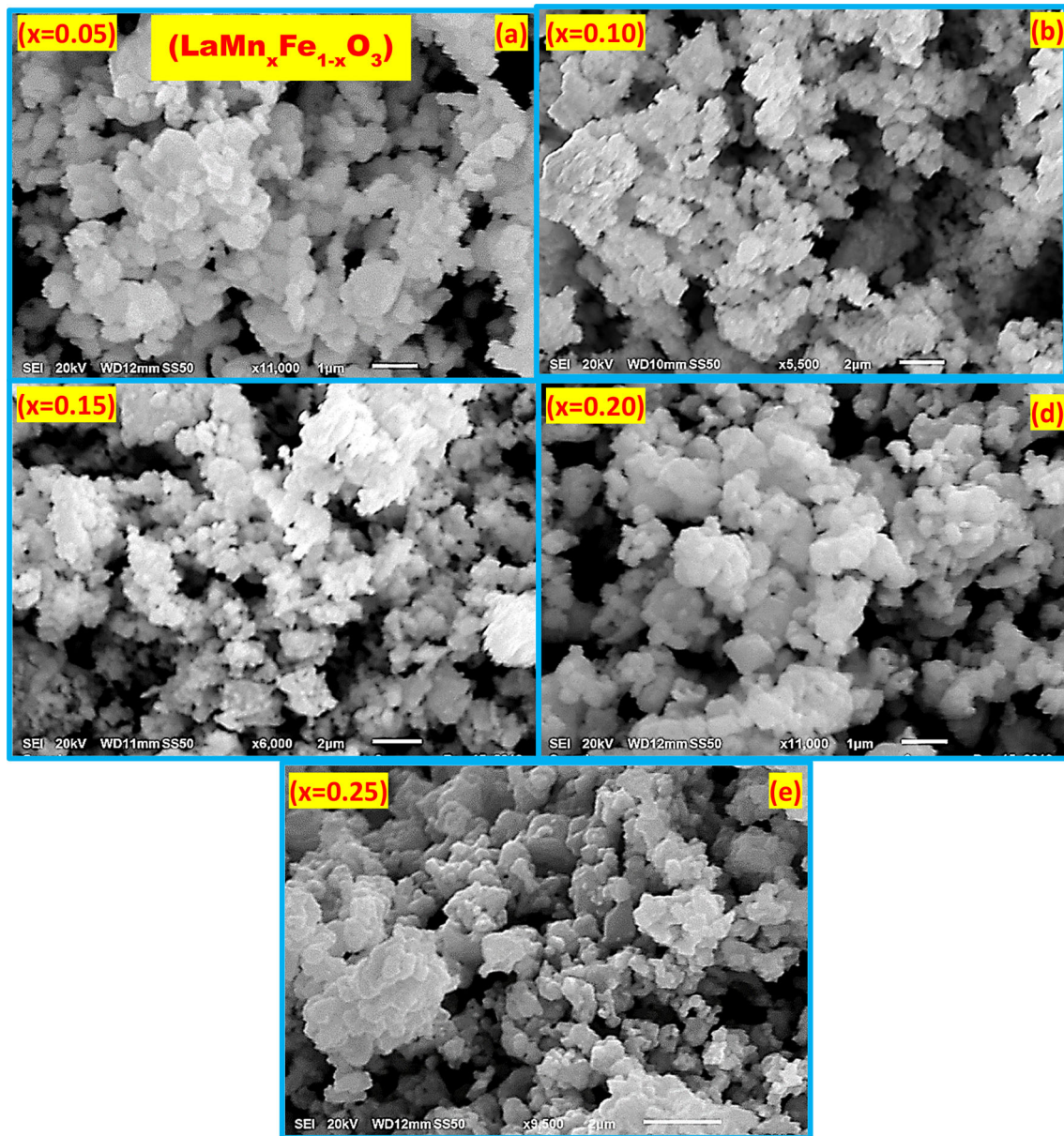


Fig. 5 SEM images and energy dispersive X-ray (EDS) pattern of the synthesized $\text{LaMn}_x\text{Fe}_{1-x}\text{O}_3$ ($x = 0.05\text{--}0.25$) ferrite materials

482 nm and 493 nm ($^1\text{S}_0 \rightarrow ^3\text{P}_1$); and 559 nm ($^1\text{S}_0 \rightarrow ^3\text{P}_0$) transitions, respectively [32]. The peak at 434 nm has a substantially higher intensity than the others, which corresponds to the emission wavelengths of near-ultraviolet (UV) chips. The strong peaks between 360 and 450 nm are due to the intra configurational f–f electronic transition of La^{3+} . The CTB excitation peak indicates the electronic excitation of $\text{O}_2\text{--La}^{3+}$ and $\text{O}_2\text{--Fe}^{3+}$, the intensity of which was the highest of any excitation peak. Furthermore, the f–f transitions demonstrate that energy is efficiently transmitted from the host to the La^{3+} ions. The

wavelength of the excitation peaks of $\text{La}^{3+}\text{--}4\text{f}$ levels, as a result, is comparable to that found in the literature [33, 34]. Figure 8 shows the electronic transitions and energy bandgap level for $\text{LaMn}_x\text{Fe}_{1-x}\text{O}_3$ ($x = 0.05\text{--}0.25$) with the index. Concerning the energy level diagram of the optical transitions within Mn, Fe ions, which is roughly illustrated by Fig. 8 (right side), such emission bands correspond to Mn, Fe, and La ion transitions, which are mostly provided by the localized transition and rare-earth 4f energy.

Figure 8 shows the red luminescence of $\text{LaMn}_x\text{Fe}_{1-x}\text{O}_3$ ($x = 0.05\text{--}0.25$) ferrite materials at the

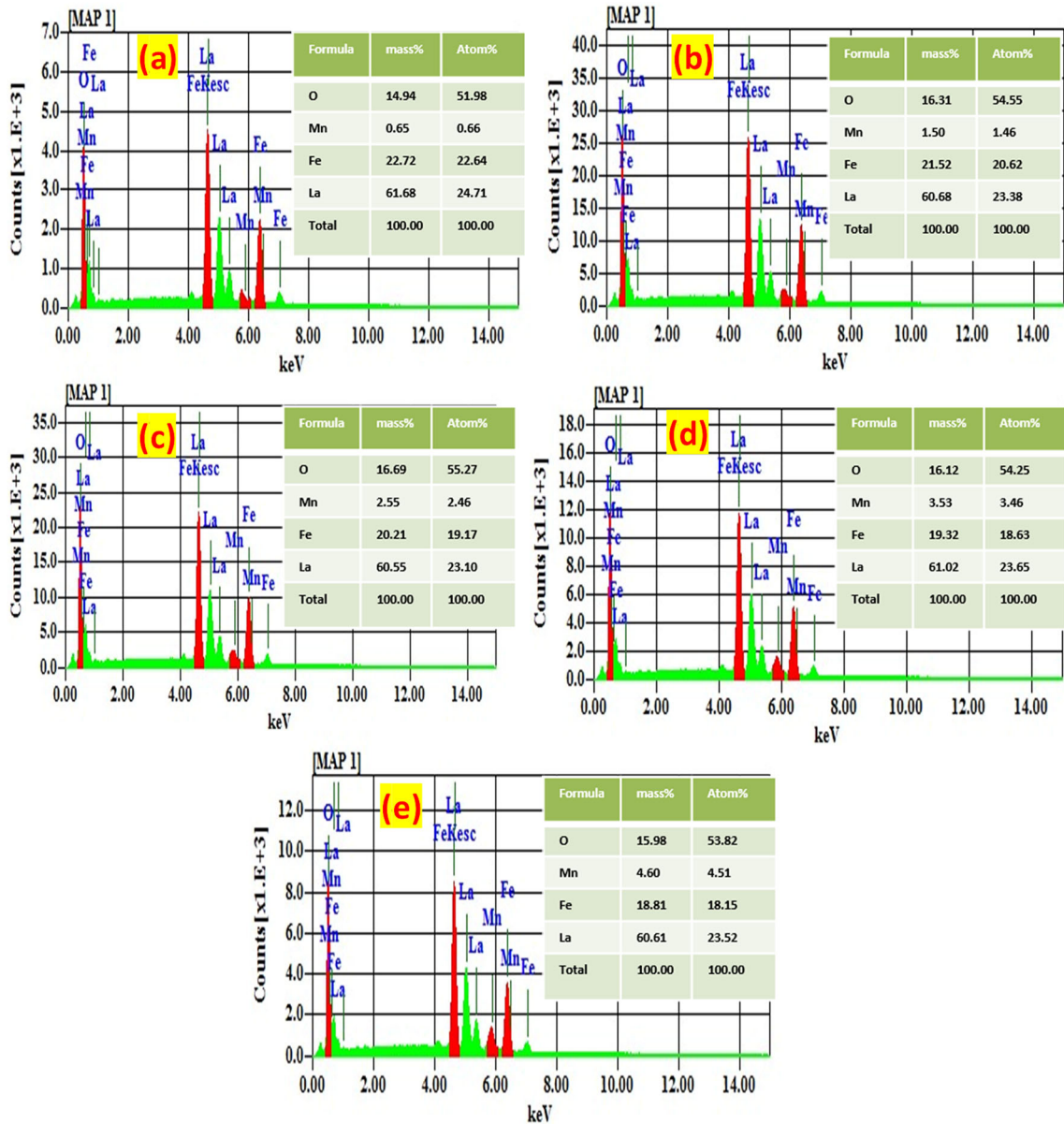


Fig. 5 continued

constructed spectra of the distinctive emission peaks of La^{3+} , as well as ${}^3\text{P}_2 \rightarrow {}^1\text{S}_0$ (409 nm), ${}^3\text{P}_1 \rightarrow {}^1\text{S}_0$ (450, 468, 482, and 492 nm), respectively. The ${}^3\text{P}_2 \rightarrow {}^1\text{S}_0$ (409 nm) and ${}^3\text{P}_1 \rightarrow {}^1\text{S}_0$ (450 nm) transitions are the most prominent of these emission peaks [30, 35]. The magnetic dipole (${}^3\text{P}_2 \rightarrow {}^1\text{S}_0$) transition is the strongest and is characterized by orange emission, whereas the electric dipole (${}^3\text{P}_1 \rightarrow {}^1\text{S}_0$) transition is characterized by red emission. The ${}^3\text{P}_2 \rightarrow {}^1\text{S}_0$ transition peak that occurs as a result of it can be assigned to the magnetic dipole (MD) transition, and the phosphor has great potential as a red phosphor for applications in near

UV chip excited WLEDs because it has a significant influence on the light output and color rendering index. The ${}^3\text{P}_2 \rightarrow {}^1\text{S}_0$ transition is well-known to be hypersensitive, which means that its intensity is highly dependent on the chemical environment. When the ion occupies a site with inversion symmetry, the intensity of ${}^3\text{P}_2 \rightarrow {}^1\text{S}_0$ increases, whereas the electric dipole transition ${}^3\text{P}_1 \rightarrow {}^1\text{S}_0$ increases when the Mn ion occupies a site without inversion symmetry. The sharpened and amplified ${}^3\text{P}_2 \rightarrow {}^1\text{S}_0$ Mn ion emissions in the LaFeO_3 host lattice indicate that the bulk of Mn ions are at inversion symmetry

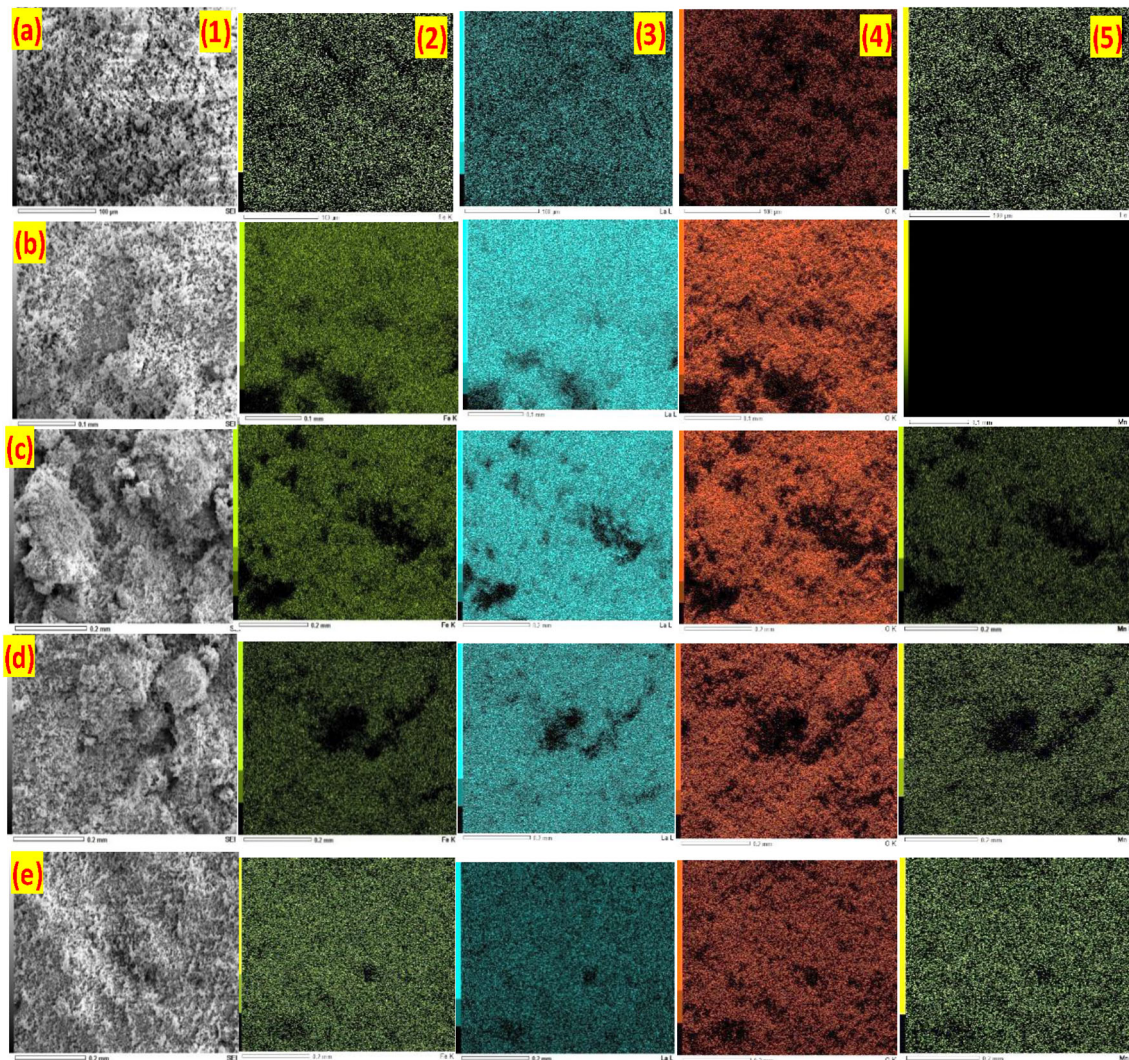


Fig. 6 Elemental mapping: column (1) the area of mapping, (2) iron distribution, (3) lanthanum distribution, (4) oxygen distribution, and (5) manganese distribution of the synthesized

$\text{LaMn}_x\text{Fe}_{1-x}\text{O}_3$ ($x = 0.05\text{--}0.25$) ferrite materials, row wise row **a** $x = 0.05$, row **b** $x = 0.10$, row **c** $x = 0.15$, **d** $x = 0.20$, and **e** $x = 0.25$

locations. The strong peaks of ${}^3\text{P}_1 \rightarrow {}^1\text{S}_0$ and ${}^3\text{P}_2 \rightarrow {}^1\text{S}_0$ electronic transitions could be attributed to localized energy transfer. These findings indicate that the good potential candidates for developing light-emitting materials (LED), optical, and photocatalytic applications [33, 36].

3.7 Dielectric property

The frequency-dependent of dielectric constant (ϵ') of the pelletized $\text{LaMn}_x\text{Fe}_{1-x}\text{O}_3$ ($x = 0.05\text{--}0.25$) ferrite materials for the frequency range from 1 kHz to 1 MHz at a various temperature range from 50 to 110

$^\circ\text{C}$ is shown in Fig. 9a–e, the inset figure shows the respective dielectric loss (δ) of the compounds. Generally, the dielectric constant is described as the response of the degree up to which the polarization of a medium is in the presence of applied electric fields. Ferric perovskite is a good dielectric

material that depends upon the distribution of cations, particle size as well as the method of synthesis. The dielectric parameters of Mn substituted LaFeO_3 have been investigated for the sol–gel synthesized materials [37]. Figure 9 shows the decrease in ϵ' with an increase in frequencies and attain a constant value at very high frequencies, and it is due

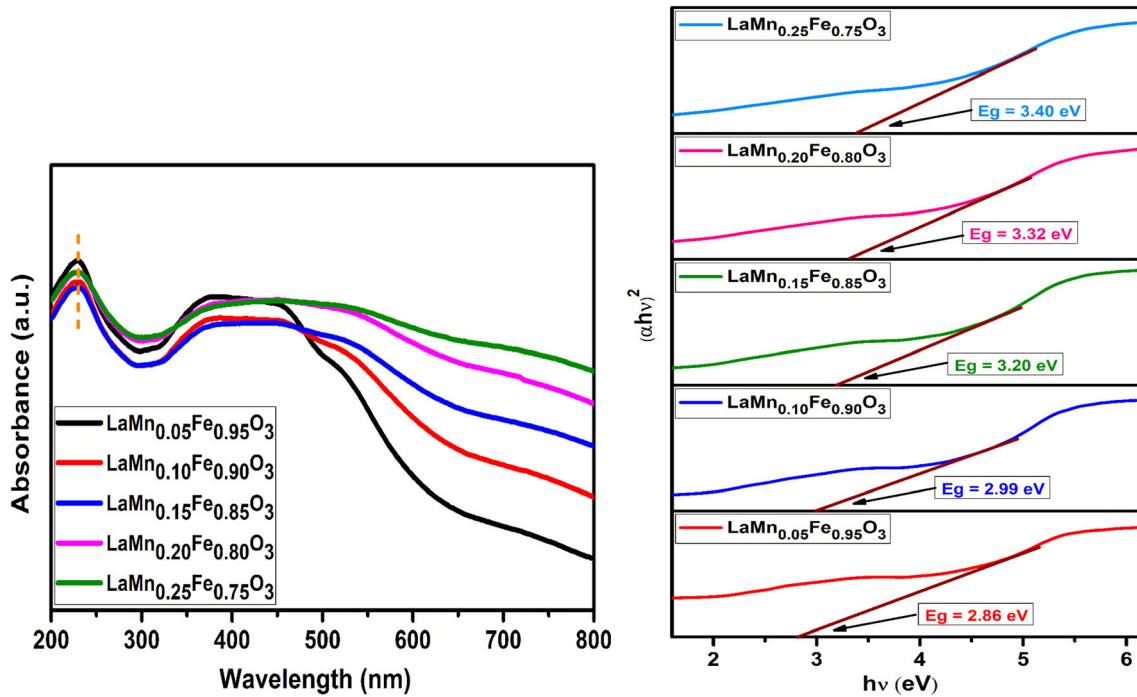


Fig. 7 UV-Vis absorbance spectra (left side) and Tauc plots of $(\alpha hv)^2$ versus photon energy (hv) (right side) of the synthesized $\text{LaMn}_x\text{Fe}_{1-x}\text{O}_3$ ($x = 0.05\text{--}0.25$) ferrite materials

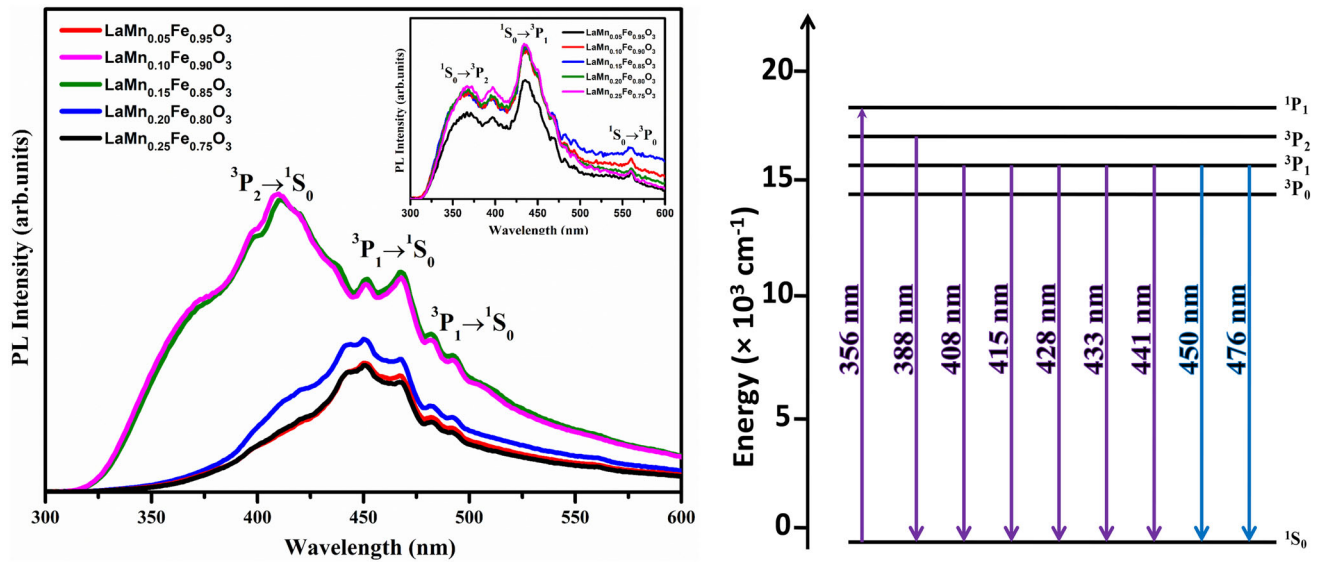


Fig. 8 The photoluminescence excitation, emission spectra (inset) and schematic energy level diagram of the optical transitions within $\text{LaMn}_x\text{Fe}_{1-x}\text{O}_3$ ($x = 0.05\text{--}0.25$) derived from using the Rare Earth Handbook [33]

to the rapid reversal of electric field in high frequencies so that no surplus ion jumps in the field direction [38]. This is generally observed in all the ferrite compounds [39, 40]. The general trend of electrical conduction and dielectric polarization is

observed similar to ferrite materials [41]. According to the Maxwell-Wagner model and Koop’s theory [42], the ferrite system is generally considered to be made up of a heterogeneous mixture of highly conducting grains that are separated by grain

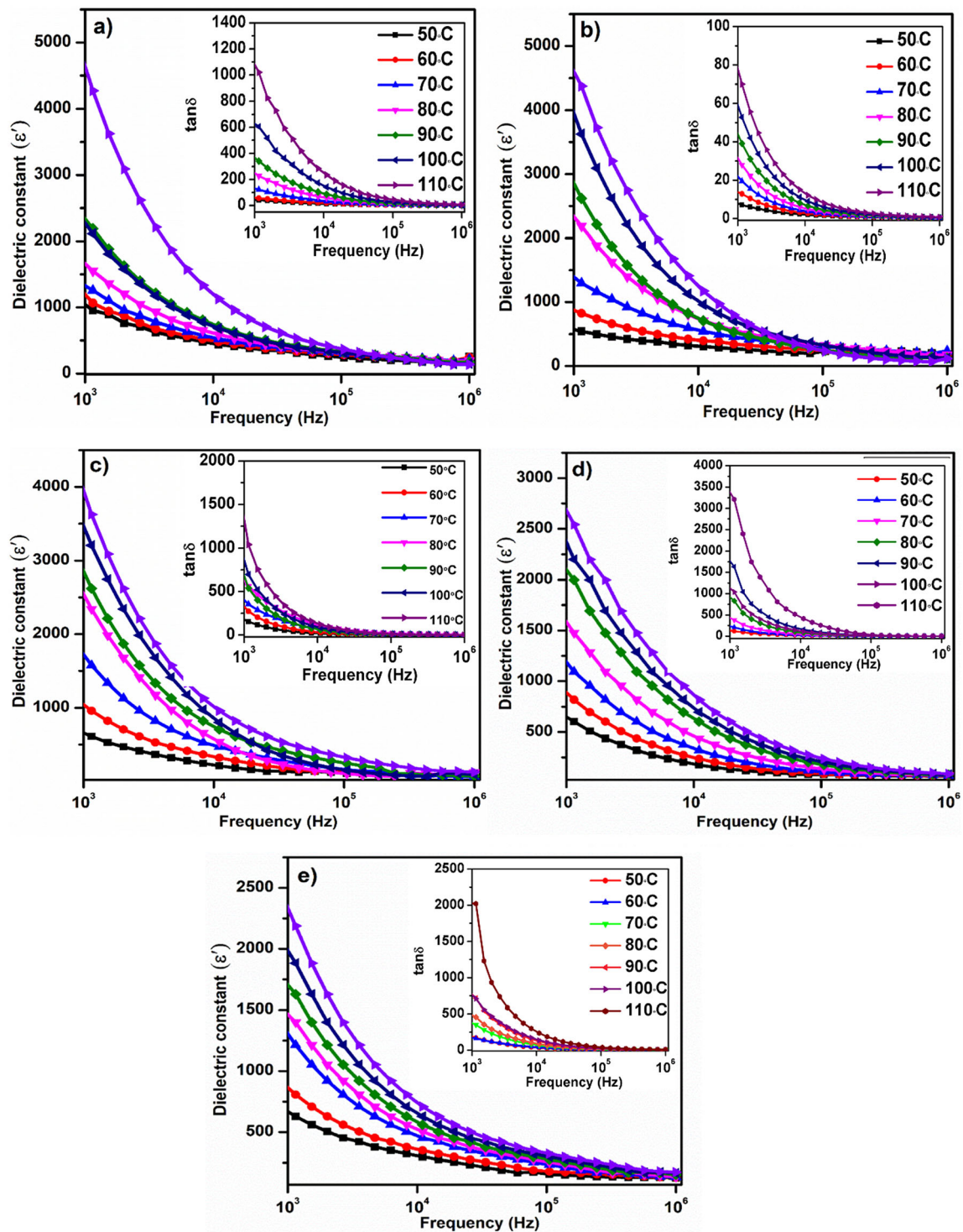


Fig. 9 Frequency dependence of dielectric constant (ϵ') (main plots) and loss tangent (δ) (inset plot) of the a–e of the synthesized $\text{LaMn}_x\text{Fe}_{1-x}\text{O}_3$ ($x = 0.05\text{--}0.25$) ferrite materials at various temperatures points

boundaries, but these grain boundaries have less conduction agree to grains. The dielectric constant increases as temperature increases as shown in Fig. 9. This dielectric constant gets increases the variation of

x composition is due to the replacement of Fe by Mn. This results in to decrease in the rate of hopping between Fe–Fe interactions. The exchange of electrons between Fe^{2+} to Fe^{3+} located at the A and B

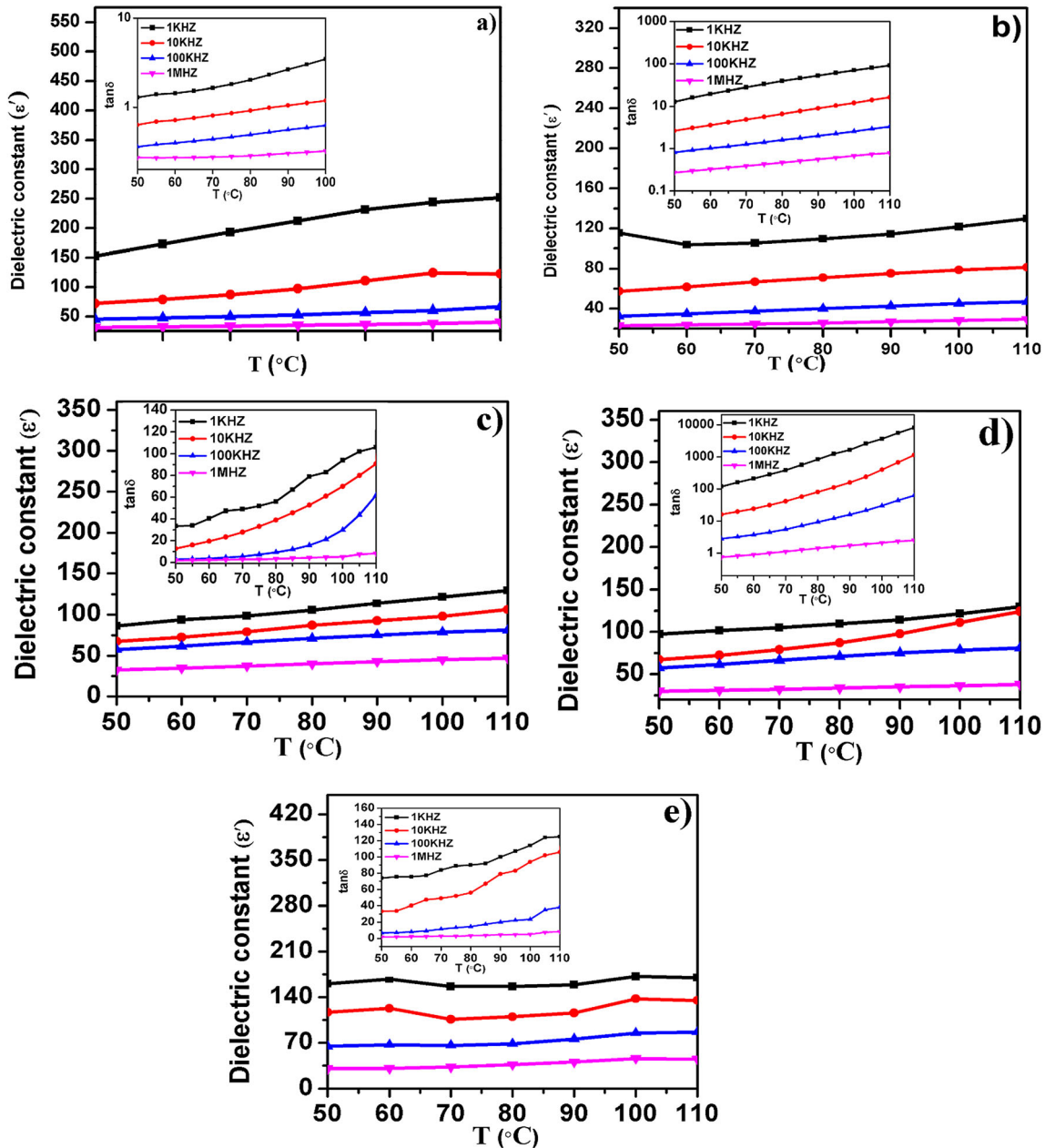


Fig. 10 Temperature dependence of dielectric constant (ϵ') and loss tangent ($\tan\delta$) (inset) at a frequency range of 1 kHz to 1 MHz of a–e $\text{LaMn}_x\text{Fe}_{1-x}\text{O}_3$ ($x = 0.05\text{--}0.25$) materials

sites of perovskites result in the dielectric polarization at higher frequencies.

The variation of dielectric loss with respect to frequency and temperature is shown in Fig. 10. The dielectric loss on frequency is generally correlated with losses by conduction. The dielectric loss increases rapidly towards the lower end of the frequency, when Mn is replaced by Fe ions the grain size decreases owing to an increase in dielectric losses

due to grain boundaries. When frequency increases the dielectric losses decrease, but the decreasing rate get decreases towards the higher frequency this effect was explained by Koop’s phenomenological theory. According to this theory, more energy is required for the conducting at grain boundaries at lower frequencies whereas very less energy is enough for the conduction at the grains [43–45].

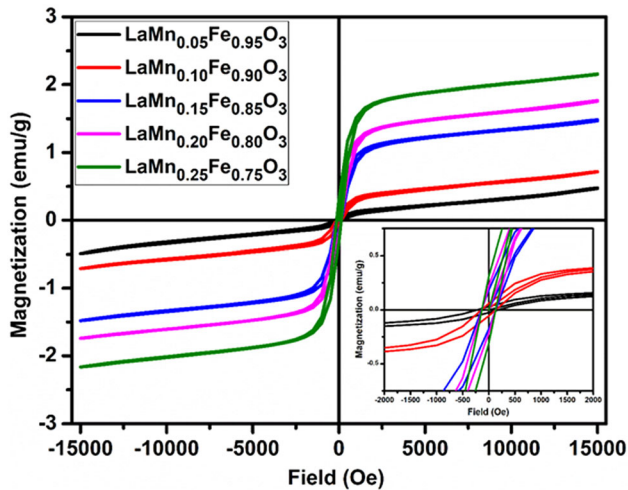


Fig. 11 Hysteresis loops of the synthesized $\text{LaMn}_x\text{Fe}_{1-x}\text{O}_3$ ($x = 0.05\text{--}0.25$) ferrite materials at room temperature

3.8 Magnetic property

Figure 11 depicts the magnetic–hysteresis (M – H) loops at room temperature as a function of applied magnetic fields for the synthesized $\text{LaMn}_x\text{Fe}_{1-x}\text{O}_3$ ($x = 0.05\text{--}0.25$) ferrite materials. The M – H loops are not saturated until the maximum field is reached at 15 kOe. Unsaturated magnetization is a frequent property of nanocrystalline materials caused by surface effects caused by small particle and crystallite sizes [46, 50]. At ambient temperature, with a Neel temperature of 740 K, virgin LaFeO_3 is reported to be canted antiferromagnetic with G-type spin orientation in which antiparallel Fe^{3+} spins interact via intervening oxygen ion [11]. The measured M – H loop for the synthesized $\text{LaMn}_x\text{Fe}_{1-x}\text{O}_3$ ($x = 0.05\text{--}0.25$) ferrite materials demonstrates a typical weak ferromagnetic response with varying degrees of magnetic strength on Mn substitution at Fe sites. The magnetic response of the produced $\text{LaMn}_x\text{Fe}_{1-x}\text{O}_3$ ferrite materials changed noticeably when Mn ions were substituted in Fe sites. Ueda et al. and Wei et al.

[12, 47] have previously reported similar phenomena. The saturation magnetization (M_s), coercivity (H_c), retentivity (M_r), and the ratio of remanence to saturation magnetization (M_r/M_s) for the synthesized $\text{LaMn}_x\text{Fe}_{1-x}\text{O}_3$ ferrite materials were determined and listed in Table 3. It demonstrates a gradual increase in M_s from 0.47 to 2.168 emu/g with concentration increases of up to 25%. In contrast, H_c is gradually decreased from 203 to 130 Oe as a function of increasing the concentration of Mn-dopant in $\text{LaMn}_x\text{Fe}_{1-x}\text{O}_3$ ferrite materials. Inset in Fig. 11 show magnified regions near the origin ($H = 0$ kOe) so that the coercivity will be more visible.

The increase in M_s for the synthesized $\text{LaMn}_x\text{Fe}_{1-x}\text{O}_3$ ferrite materials might be attributable to two factors. First, there is a mismatch between two magnetic sublattices caused by the presence of Fe/Mn on substitution, which distorts the Fe/MnO_6 octahedra and causes a visible change in the Fe/Mn-O-Fe/Mn bond angle, reinforcing magnetic strength. Such a potential appears logical and clear from Rietveld’s refinement of XRD results. A systematic increase (Table 1) in in-plane $\text{Fe/Mn-O}_1\text{-Fe/Mn}$ bond angle and out-of-plane $\text{Fe/Mn-O}_2\text{-Fe/Mn}$ bond angle up to 25% concentration improves the M_s . This finding is supported by a similar change in the Fe/Mn-O-Fe/Mn bending mode in the FTIR spectrum. As a result, the concentration-dependent tunability of M_s is caused mostly by the strong M–O interaction on substitution. The second possibility is that the mixed-valence state of Mn ions (+ 3/ + 4) produces double exchange contacts ($\text{Fe}^{3+}\text{-O-Mn}^{3+}$, $\text{Mn}^{3+}\text{-O-Mn}^{4+}$) in the lattice, resulting in weak ferromagnetism with increasing Mn concentration. The superexchange mechanisms of $\text{Fe}^{3+}\text{-O-Fe}^{3+}$ and $\text{Fe}^{3+}\text{-O-Mn}^{3+}$ are antiferromagnetic according to the Goodenough–Kanamori criteria, whereas the superexchange mechanism of $\text{Fe}^{3+}\text{-O-Mn}^{4+}$ is ferromagnetic [49]. The possibility of superexchange interaction ($\text{Mn}^{3+}\text{-}$

Table 3 Magnetic parameters of the synthesized $\text{LaMn}_x\text{Fe}_{1-x}\text{O}_3$ ($x = 0.05\text{--}0.25$) ferrite materials

$\text{LaMn}_x\text{Fe}_{1-x}\text{O}_3$ ($x = 0.05\text{--}0.25$)	M_s (emu/g)	M_r (emu/g)	M_r/M_s	η_B (μ_B)	H_c (Oe)	Anisotropy constant, K (Oe)
0.05	0.470	0.029	0.062	0.020	203	99
0.10	0.710	0.057	0.080	0.030	136	100
0.15	1.475	0.174	0.118	0.064	135	207
0.20	1.753	0.221	0.126	0.076	131	236
0.25	2.168	0.290	0.134	0.094	130	293

O–Mn³⁺, Mn⁴⁺–O–Mn⁴⁺) in the system, however, cannot be ruled out. Furthermore, due to the high Mn content in LaFeO₃ ($x = 0.25$), antiferromagnetic interactions of Mn³⁺–O–Mn³⁺ or Mn⁴⁺–O–Mn⁴⁺ may occur, resulting in a decrease in M_s , implying a decrease in ferromagnetism in strongly substituting ferrite compounds.

The M_r is an independent parameter since it is not entirely dependent on M_s and H_c . Table 3 lists the values of M_r derived from the M – H loop for the synthesized LaMn _{x} Fe_{1– x} O₃ ($x = 0.05$ – 0.25) ferrite materials. This value of M_r agreed well with earlier literature [47, 48]. With a rise in Mn-dopant content, M_r increases from 0.029 to 0.29 emu/g. This rise in M_r is attributable to an increase in saturation magnetization for the LaMn _{x} Fe_{1– x} O₃ ($x = 0.05$ – 0.25) ferrite materials that were produced.

Using M_s and M_r data, the squareness ratios for the synthesized LaMn _{x} Fe_{1– x} O₃ ($x = 0.05$ – 0.25) ferrite materials were computed using the equation below, Squareness ratio = M_r/M_s (5)

The Stoner–Wohlfarth model predicts that the squareness ratio of 3D random particles is $M_r/M_s = 0.5$ for uniaxial anisotropy and $M_r/M_s = 0.83$ for cubic anisotropy [51]. In the current investigation, the M_r/M_s values for all of the synthesized ferrite materials are less than 0.5, as shown in Table 3. As a result, all of the materials are in good agreement with uniaxial anisotropy (< 0.5) than cubic anisotropy.

Magnetic moment per formula unit in a Bohr magnetron (μ_B) for the synthesized LaMn _{x} Fe_{1– x} O₃ ($x = 0.05$ – 0.25) ferrite materials were determined using the equation [51],

$$\mu_B = M * M_s / 5585 \quad (6)$$

where M stands for molecular weight and M_s stands for saturation magnetization (emu/g). Table 3 shows the observed magnetic moment values as a function of Mn concentration x . It demonstrates that when Mn ions are substituted for Fe ions in lanthanum ferrite, the measured magnetic moment increases due to the strengthening of the A–B superexchange contacts between the cationic ions.

From the relationship, the magnetic anisotropy constant (K) of the produced LaMn _{x} Fe_{1– x} O₃ ($x = 0.05$ – 0.25) ferrite materials may be computed,

$$K = H_c * M_s / 0.98 \quad (7)$$

Table 3 shows the behavior of K concerning Mn-dopant during the synthesis of LaMn _{x} Fe_{1– x} O₃ materials. Table 3 shows that the K increases as the Mn-dopant increases. This rise could be related to the H_c and M_s values. It is proposed that by adjusting the concentration of dopant, LaMn _{x} Fe_{1– x} O₃ ferrite materials with variable magnetic properties may be designed, which might be used as a promising option for gas sensing, magnetic memory storage, high-frequency switching, and applications.

4 Conclusion

This work provides a strategy to tune the properties of lanthanum ferrite utilizing Mn substitution. Upto Mn-doping, the red photoluminescence properties were enhanced with near-UV light at 409 nm. Mn-dopant has a significant influence on dielectric characteristics in the frequency ranges of 1 kHz and 1 MHz from 50 to 110 °C, which obey the Maxwell–Wagner polarization model and Koop's phenomenological theory. Magnetic investigations at 305 K show an increase in magnetic response, M_s (2.17 emu/g), for $x = 0.25\%$ mol of Mn in LaMn _{x} Fe_{1– x} O₃, where this material effectively offers a new functional perspective for the creation of magnetic memory devices.

References

1. S.K. Kundu, D.K. Rana, A. Banerjee, D. Das, S. Basu, Mater. Res. Express **6**, 085032 (2019)
2. K.K. Bhargav, A. Maity, S. Ram, S.B. Majumder, Sens. Actuators B **195**, 303 (2014)
3. T. Hibino, S. Wang, S. Kakimoto, M. Sano, Solid State Ion. **127**, 89 (2000)
4. H. Zhang, P. Song, D. Han, Q. Wang, Physica E **63**, 21 (2014)
5. K. Huang, H.Y. Lee, J.B. Goodenough, J. Electrochem. Soc. **145**, 3220 (1999)
6. M.H. Hung, M.V.M. Rao, D.S. Tsai, Mater. Chem. Phys. **101**, 297 (2007)
7. A. Delmastro, D. Mazza, S. Ronchetti, M. Vallino, R. Spinicci, P. Brovetto, M. Salis, Mater. Sci. Eng. B **79**, 140 (2001)
8. D. Wang, M. Gong, J. Appl. Phys. **109**, 114304 (2011)
9. Y.S. Didosyan, H. Hauser, IEEE Trans. Instrum. Meas. **49**, 14 (2000)

10. Y.S. Didosyan, H. Hauser, W. Fiala, J. Nicolics, W. Toriser, J. Appl. Phys. **91**, 7000 (2002)
11. S. Acharya, J. Mondal, S. Ghosh, S.K. Roy, P.K. Chakrabarti, Mater. Lett. **64**, 415 (2010)
12. K. Ueda, T. Tabata Hand Kawai, Phys. Rev. B **60**, R12561 (1999)
13. Z.X. Wei, Y. Wang, J.P. Liu, C.M. Xiao, W.W. Zeng, Mater. Chem. Phys. **136**, 755 (2012)
14. R. Dhahri, M. Bejar, M. Hajlaoui, N. Sdiri, M.A. Valente, E. Dhahri, J. Magn. Magn. Mater. **321**, 1735 (2009)
15. P.P. Hankarea, M.R. Kadama, P.D. Kambale, S.D. Jadhava, U.B. Sankpala, R.P. Patil, V.B. Helavia, N.S. Gajbhiyeb, J. Alloys Compd. **489**, 233 (2010)
16. C. Zeng, Y. He, C. Li, Y. Xu, Ceram. Int. **39**, 5765 (2013)
17. J.H. Jeong, C.G. Song, K.H. Kim, W. Sigmund, J.W. Yoon, J. Alloys Compd. **749**, 599 (2018)
18. W. Tong, B. Zhang, S. Tan, Y. Zhang, Phys. Rev. B **70**, 014422 (2004)
19. R.D. Shannon, Acta Crystallogr. A **32**, 751 (1976)
20. D. Triyono, H. Laysandra, L.H. Liu, A.W. Anugrah, J. Mater. Sci. Mater. Electron. **30**, 18584 (2019)
21. A.L. Patterson, Phys. Rev. **56**, 978 (1939)
22. G.V.S. Rao, C.N.R. Rao, J.R. Ferraro, Appl. Spectrosc. **24**, 436 (1970)
23. K. Sultan, M. Ikrama, K. Asokan, Vacuum **99**, 251 (2014)
24. R.P.S.M. Lobo, R.L. Moreira, D. Lebeugle, D. Colson, Phys. Rev. B **76**, 172105 (2007)
25. M.N. Iliiev, M.V. Abrashev, H.-G. Lee, V.N. Popov, Y.Y. Sun, C. Thomsen, R.L. Meng, C.W. Chu, Phys. Rev. B **57**(5), 2872 (1998)
26. M.C. Weber, M. Guennou, H.J. Zhao, J. Iniguez, R. Vilarinho, A. Almeida, J.A. Moreira, J. Kreise, Phys. Rev. B **94**, 214103 (2016)
27. S. Merten, V.B. Bamberg, B. Damaschke, K. Samwer, V. Moshnyaga, Phys. Rev. Mater. **3**, 060401 (2019)
28. G.S. Babu, V. Subramanian, V.R.K. Murthy, R.L. Moreira, R.P.S.M. Lobo, J. Appl. Phys. **103**, 084104 (2008)
29. P. Shikha, T.S. Kang, B.S. Randhawa, J. Alloys Compd. **625**, 336 (2015)
30. R. Marschall, J. Soldat, M. Wark, Photochem. Photobiol. Sci. **12**, 671 (2013)
31. E. Swatsitang, A. Karaphun, S. Phokha, S. Hunpraturb, T. Putjuso, J. Sol-Gel Sci. Technol. **81**, 483 (2017)
32. B.M. Jaffar, H.C. Swart, H.A.A. Seed Ahmed, A. Yousif, R.E. Kroon, J. Lumin. **209**, 217 (2019)
33. R. Jbeli, A. Boukhachem, F. Saadallah, S. Alleg, M. Amlouk, H. Ezzaouia, Mater. Res. Express **6**, 066414 (2019)
34. R. Jbeli, A. Boukhachem, I. Ben Jemaa, N. Mahdhi, F. Saadallah, H. Elhouichet, S. Alleg, M. Amlouk, H. Ezzaouia, Spectrochim. Acta A **184**, 71 (2017)
35. K. Li, D. Wang, F. Wu, T. Xie, T. Li, Mater. Chem. Phys. **64**, 269 (2000)
36. J.Y. Li, *Luminescent Materials of Rare Earths and Their Applications* (Chemical Industry Press, Beijing, 2003), p. 8
37. A.W. Anugrah, D. Triyono, H. Laysandra, IOP Conf. Ser. Mater. Sci. Eng. **496**, 012033 (2019)
38. S.V. Rathan, G. Govindaraj, Solid State Sci. **12**(5), 730 (2010)
39. G.R. Mohan, D. Ravinder, A.V.R. Reddy, B.S. Boyanov, Mater. Lett. **40**, 39 (1999)
40. L.I. Rabinkin, Z.I. Novikova, *Ferrites* (Doklady Akademii Nauk SSSR, Minsk, 1960), p. 146
41. M. Bakr Mohamed, H. Wang, H. Fuess, J. Phys. D **43**, 455409 (2010)
42. C.G. Koops, Phys. Rev. **83**, 121 (1951)
43. J.C. Maxwell, *Electricity and Magnetism*, vol. 1 (Oxford University Press, New York, 1973), p. 828
44. J. Chand, M. Singh, J. Alloys Compd. **486**, 376 (2009)
45. M. Ishaque, M.U. Islam, M. Azhar Khan, I.Z. Rahman, A. Genson, S. Hampshire, Physica B **405**, 1532 (2010)
46. R. Singh, Y. Jaromir, H. Ivo, Z. Kozakova, M. Palou, E. Barton, J. Masilko, L. Kalina, M. Hajd, J. Supercond. Nov. Magn. **28**, 2097 (2015)
47. Z.X. Wei, Y. Wang, J.P. Liu, C.M. Xiao, W.W. Zeng, S.B. Ye, J. Mater. Sci. **48**, 1117 (2013)
48. S.D. Bham, V.L. Joseph Joly, P.A. Joy, Phys. Rev. B **72**, 054426 (2005)
49. P. Shikha Komal, T.S. Kang, B.S. Randhawa, J. Alloys Compd. **701**, 788 (2017)
50. J. Murbe, J. Topfer, J. Eur. Ceram. Soc. **32**, 1091 (2012)
51. E.C. Stoner, E.P. Wohlfarth, Philos. Trans. R. Soc. Lond. A **240**, 599 (1948)

Publisher's Note Springer Nature remains neutral with regard to jurisdictional claims in published maps and institutional affiliations.